ADVANCING EARTH AND SPACE SCIENCE

JGR Space Physics

RESEARCH ARTICLE
10.1029/2023JA031352

Key Points:

- An updated reconstruction of the monthly heliospheric modulation potential is derived for 1964–2022
- A new unique daily-resolution version of the heliospheric modulation potential is presented
- The stability of individual neutron monitors is assessed for 1964–2022

Supporting Information:

Supporting Information may be found in the online version of this article.

Correspondence to:

P. Väisänen,
pauli.vaisanen@oulu.fi

Citation:

Väisänen, P., Usoskin, I., Kähkönen, R., Koldobskiy, S., & Mursula, K. (2023). Revised reconstruction of the heliospheric modulation potential for 1964–2022. *Journal of Geophysical Research: Space Physics*, *128*, e2023JA031352. https://doi.org/10.1029/2023JA031352

Received 31 JAN 2023
Accepted 27 MAR 2023

Revised Reconstruction of the Heliospheric Modulation Potential for 1964–2022

Pauli Väisänen[1], Ilya Usoskin[1,2], Riikka Kähkönen[1], Sergey Koldobskiy[1,2], and Kalevi Mursula[1]

[1]Space Physics and Astronomy Research Unit, University of Oulu, Oulu, Finland, [2]Sodankylä Geophysical Observatory, University of Oulu, Oulu, Finland

Abstract Galactic cosmic rays (GCRs) impinge on the Earth's atmosphere and generate showers of secondary particles in nuclear collisions with the atmospheric constituents. The flux of GCR near Earth is subjected to heliospheric modulation driven by solar magnetic activity and to geomagnetic shielding. Variability of the GCR flux is continuously monitored by the worldwide network of ground-based neutron monitors (NMs) since the 1950s. Solar modulation is often quantified via the force-field approximation parameterized by the modulation potential ϕ, which can be evaluated from the global NM data set. Here we revisit the methodology and provide an updated and extended reconstruction of the heliospheric modulation potential for 1964–2022, using a recent NM yield function and the measurements of the 10 most stable high-latitude NMs. A key improvement in the reconstructed heliospheric modulation potential is the new daily resolution, which provides new opportunities for further research. Reconstruction uses the root-mean square error (RMSE) minimization to find the optimum daily and monthly scaling factors for individual NMs. The stability of the reconstruction is analyzed and the errors are estimated. The mean level of uncertainty is low, generally within $\pm 1\%$, but it is found to depict marginal variability at the 11-year, annual and 27-day timescales at the $<1\%$ level, indicating that a very small systematic uncertainty is still present.

1. Introduction

While the flux of galactic cosmic rays (GCRs) in the local interstellar medium is considered to be roughly constant on decadal to millennial timescales, it varies significantly in the vicinity of the Earth because of the modulation in the heliosphere. Studying this modulation forms an important subject for solar and heliospheric physics and for terrestrial and technological aspects of cosmic-ray induced effects. GCR variability is continuously measured by ground-based neutron monitors (NMs) since the 1950s (e.g., Simpson, 2000), that is, continuously during seven decades. Although a single NM station cannot measure the energy spectrum of cosmic rays, the global network of NMs covering different locations around the globe can act as a large-scale spectrometer (Bieber et al., 2004) and provide an estimate of the GCR energy spectrum.

Although the process of cosmic-ray modulation in the heliosphere is very complex (e.g., Engelbrecht et al., 2022; Potgieter, 2013), it is often approximated, especially for practical purposes, via the so-called force-field parameterization quantified by a single parameter, the so-called modulation potential ϕ, which is determined by solar magnetic activity (e.g., Caballero-Lopez & Moraal, 2004; Gleeson & Axford, 1968; Usoskin et al., 2005). The modulation potential is usually evaluated based on the data from multiple NMs using the method initially proposed by Usoskin et al. (2005) and developed further by Usoskin et al. (2011, 2017).

Here we critically revise and update the NM-based reconstruction of the modulation potential for the five last solar cycles by employing an updated methodology, an upgraded model of the NM yield function (Mishev et al., 2020) and a new verified set of NM data (Väisänen et al., 2021). For the first time, we provide the modulation potential at daily time resolution, while earlier NM-based reconstructions (Usoskin et al., 2005, 2011, 2017) had monthly or yearly resolution. The results are provided in the form of computer-readable tables along with an algorithm, making it possible to extend the published data set when new data appear. The new data set is useful for space weather, space climate, as well as solar and heliospheric physics.

2. Methods and Data

2.1. Modulation Potential

GCRs are modulated in the heliosphere by solar magnetic activity (see, e.g., a review by Potgieter, 2013). The main processes driving the modulation are convection by radially expanding solar wind, scattering on magnetic irregularities, large-scale drifts due to an inhomogeneous heliospheric magnetic field, including the heliospheric current sheet, and adiabatic cooling. In addition, interplanetary propagating barriers in the form of interaction regions and shocks dominate the short-term modulation around solar cycle maxima. This leads to the prominent 11-year solar cycle in the intensity of GCRs as measured on the Earth. In addition to the slow variation over the cycle, fast and strong suppressions of the GCR flux, known as Forbush decreases (FDs) also appear as a result of interplanetary transients (e.g., Dumbović et al., 2022). The effect of drift is charge-sign dependent, which leads to the alternation of flat and sharp peaks of 11-year cycles and a related 22-year quasi-cycle in GCR intensity (e.g., Jokipii & Levy, 1977).

Full modeling of GCR modulation requires a complicated numerical solution of the transport equation (Parker, 1965) with many unknown parameters such as the diffusion tensor (e.g., Engelbrecht et al., 2022) which cannot be directly measured nor even inferred. Accordingly, the GCR flux at 1 AU is often estimated by employing the so-called "force-field" approximation (Caballero-Lopez & Moraal, 2004; Gleeson & Axford, 1968; Usoskin et al., 2005) which, while not providing insights to the physical processes, offers a good single-parameter parameterization of the GCR spectra near Earth with a reasonable accuracy of 10%–20% (Corti et al., 2016; Koldobskiy et al., 2019). This approximation is particularly useful for long-term studies and practical/applied purposes where high accuracy or full modeling is not necessary or even possible.

In the framework of the force-field approximation, the energy spectrum of the ith GCR species (characterized by atomic A_i and charge Z_i numbers) near Earth is related to the (assumed to be constant) local interstellar spectrum (LIS) outside of the heliosphere $J_{\mathrm{LIS},i}$, as

$$J_i(T,\phi) = J_{\mathrm{LIS},i}(T+\Phi_i)\frac{(T)(T+2T_{\mathrm{r}})}{(T+\Phi_i)(T+\Phi_i+2T_{\mathrm{r}})}, \tag{1}$$

where ϕ is the modulation potential, $\Phi_i = (eZ_i/A_i)\phi$, T is the kinetic energy per nucleon, and T_{r} is the rest mass energy per nucleon (0.938 GeV for protons, 0.932 GeV for alpha particles). Energies are given in electron volts and the modulation potential in volts. Formally, the modulation potential corresponds to the mean energy loss Φ of an energetic charged particle in the heliosphere before it can reach the Earth's orbit.

The only variable parameter in Equation 1 is the modulation potential ϕ, which is usually defined empirically from in-situ measurements of the GCR spectrum or from ground-based measurements by NMs. As a reference series, we use the monthly values of the modulation potential ϕ from Usoskin et al. (2017) (hereafter U17), available at https://cosmicrays.oulu.fi/phi/phi.html.

After 2017, this series was continuously extended using a simplified method employing data from only a few NM (see discussion below) and, accordingly, is less accurate than before 2017.

The exact values of ϕ slightly depend on the form of LIS but can be straightforwardly reduced to each other (Herbst et al., 2010; Usoskin et al., 2005). Here we employ the LIS provided by Vos and Potgieter (2015):

$$J_{\mathrm{LIS}}(T) = C_i \cdot 2700 \cdot \frac{T^{1.12}}{\beta^2}\left(\frac{T+0.67}{1.67}\right)^{-3.93}, \tag{2}$$

where β is the ratio of the particle's velocity to the speed of light, and J and T are given in (m^2 s sr GeV/nuc)$^{-1}$ and GeV/nuc, respectively. The factor C_i is the ratio of different GCR species to that of protons (see Koldobskiy et al., 2019), $C_p = 1$ for protons and

$$C_\alpha = 4.3 \cdot 10^{-9}\phi^2 - 6.2 \cdot 10^{-7}\phi + 0.337 \tag{3}$$

for α-particles (which effectively includes also heavier $Z > 2$ species), where ϕ is in MV. Cosmic-ray intensities are given in units of particles/(m^2 sr s GeV/nuc) and energy in GeV.

2.2. NM Count Rate

A NM is an energy-integrating detector of cosmic rays. Its count rate is defined not only by the spectrum of GCR near the Earth but also by the altitude (quantified by the residual atmospheric depth h) and geographical location, quantified by the geomagnetic cutoff rigidity R_c (Cooke et al., 1991) of the NM location. The theoretical count rate of a NM (denoted henceforth as N^*) with the geomagnetic rigidity cutoff R_c and atmospheric depth h at time t can be computed as

$$N^*(R_c, h, t) = \sum_i \int_{T_{c,i}}^{\infty} Y_i(T, h)\, J_i(T, \phi(t))\, dT, \tag{4}$$

where $T_{c,i} = \sqrt{(Z_i \cdot R_c/A_i)^2 + T_r^2} - T_r$ is the CR particle's minimum kinetic energy needed to reach the NM location with R_c, $Y_i(T, h)$ is the NM yield function, $J_i(T, \phi(t))$ is the energy spectrum of CR particles of type i as defined by Equations 1–3, and summation is over different types of CR particles (here we consider only protons and α-particles, which contain heavier species via C of Equation 3).

Here we use the NM yield functions $Y_i(T, h)$ as calculated and presented recently by Mishev et al. (2020) separately for protons and α-particles. The yield function is parameterized so that the altitude dependence at any given atmospheric depth h is reduced to the reference depth $h = 1{,}000$ g/cm^2, which is close to the sea-level atmospheric thickness of 1,033 g/cm^2:

$$\ln\left(\frac{Y(h,T)}{Y(1000,T)}\right) = A(R_p)\cdot(1000-h)^2 + B(R_p)\cdot(1000-h), \tag{5}$$

where parameter $R_p = \sqrt{T\cdot(T+2T_r)}$ is the proton rigidity. Coefficients $A(R)$ and $B(R)$ are defined as

$$A(R_p) = \sum_{l=0}^{5} b_l(\ln(R_p))^l \tag{6}$$

$$B(R_p) = \sum_{l=0}^{5} b_l(\ln(R_p))^l \tag{7}$$

where coefficients b_l for terms A and B separately can be found in Table 4 of Mishev et al. (2020). The reference yield function at 1,000 g/cm^2 is parameterized as

$$\ln(Y(1000,T)) = \sum_{l=0}^{3} a_l(\ln(R))^l. \tag{8}$$

where coefficients a_l for different energy ranges for protons and α-particles can be found in Table 3 of Mishev et al. (2020).

An example of the theoretical count rate of a standard 6-counter NM64 station at atmospheric depth $h = 1{,}020$ g/cm^2 is shown in Figure 1 as a function of the modulation potential ϕ and the geomagnetic rigidity cutoff R_c.

Theoretical count rates for the 10 NMs (see Table 1) whose data are used here, are shown in Figure 2 as a function of the modulation parameter. Count rates are calculated using the respective atmospheric depth and cut-off rigidity given in Table 1. Sanae64 count rate is high because of the high altitude and latitude of the station.

2.3. NM Selection

We base our analysis on the most stable NMs called primary NMs (Väisänen et al., 2021). These primary NMs were selected as long-operating stations without apparent significant errors or jumps in their efficiency throughout their operation periods. Times of ground level enhancement (GLE) events (Poluianov et al., 2017) were excluded according to the GLE list available at https://gle.oulu.fi/. Their exact times are available in Table S3. Obvious outliers or jumps were also excluded or corrected. We focus our analysis on 10 primary NMs with low cut-off rigidity $R_c \leq 3$ GV, which have higher count rates and are more affected by the heliospheric modulation and thus are better suited, in the sense of the signal-to-noise ratio, to reconstruct the modulation potential (e.g., Usoskin et al., 2017). We further require that the used NMs should have a data coverage of at least 85% between the years 1964–2021. Since different NMs have different number of counters, we normalize all count rates to the

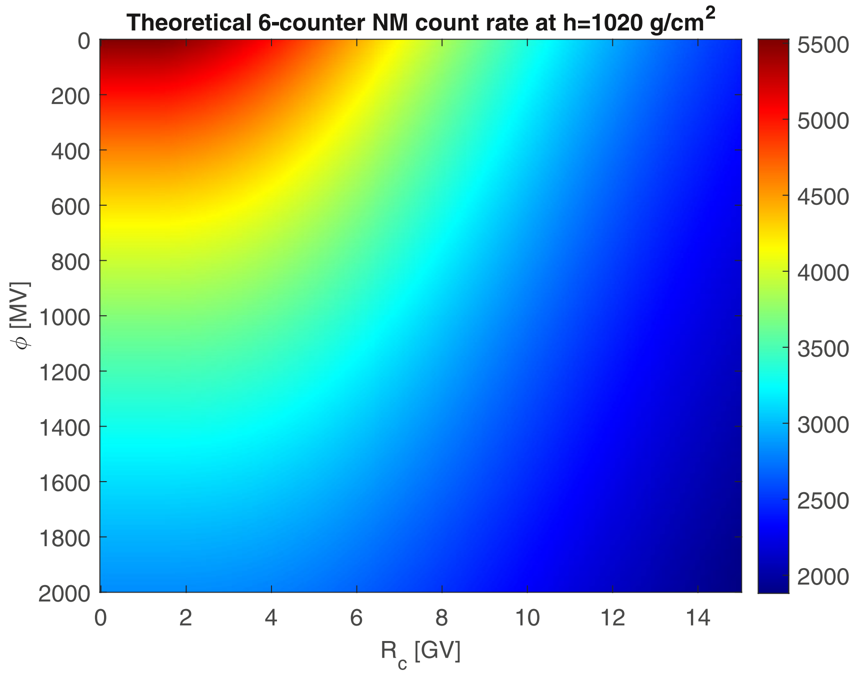

Figure 1. Theoretical count rate N^* [counts/min] of a standard 6NM64 monitor at the atmospheric depth h = 1,020 g/cm^2 as a function of the modulation potential ϕ and the geomagnetic rigidity cutoff R_c.

standard 6NM64. This leads to the list of 10 primary NMs as presented in Table 1. Their count rates are shown in Figure 3. The black curve denotes the station coverage.

Table 1 also lists the average cutoff rigidities R_c computed using the PLANETOCOSMICS code (Desorgher et al., 2005), with the TS89 external magnetic field model (Tsyganenko, 1989) for quiet magnetosphere conditions (Kp = 0). For the actual computations, gradual changes in R_c were taken into account by using the IGRF (International Geomagnetic Reference Field—Alken et al., 2021) model with 5-year epochs and linear interpolations between them.

2.4. Scaling Factors

While theoretical count rates N^* are computed for an ideal detector, real NMs may differ from the ideal one, for example, due to local surrounding, electronic setup, data acquisition etc. Here we compare the theoretical N^* (as

Table 1
List of Primary Neutron Monitors Analyzed Here

Station	Latitude	Longitude	h (g/cm^2)	R_c (GV)	# of counters	$\kappa \pm \sigma_\kappa$
Inuvik	68.35	−133.72	1030.51	0.21	18	1.764 ± 0.011
Kerguelen	−49.35	70.27	1019.63	1.03	18	0.984 ± 0.009
Kiel	54.3	10.1	1026.43	2.22	18	1.192 ± 0.014
McMurdo	−77.95	166.6	1026.85	0	18	1.287 ± 0.016
Moscow	55.47	37.32	1019.72	2.23	24	1.885 ± 0.016
Newark	39.7	−75.7	1032.97	2.10	9	1.033 ± 0.005
Novosibirsk	54.48	83	1014.62	2.64	24	1.575 ± 0.025
Oulu	65.05	25.47	1019.72	0.65	9	1.022 ± 0.008
Sanae64	−71.67	−2.85	897.28	0.67	6	1.747 ± 0.014
Thule	76.5	−68.7	1025.07	0	18	1.688 ± 0.021

Note. Columns are: (1) station name, (2, 3) geographic coordinates in degrees, (4) atmospheric depth, (5) cut-off rigidity R_c, (6) the number of counters, and (7) the mean scaling factor with it standard deviation.

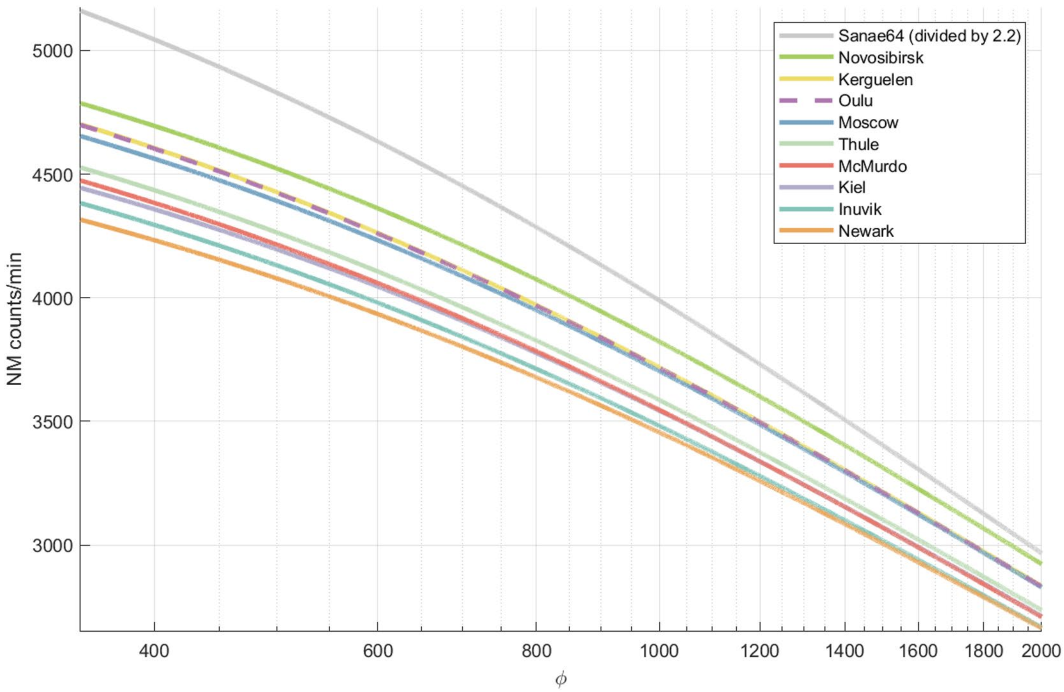

Figure 2. Theoretical count rates N^* (reduced to the 6NM64 standard) of the 10 neutron monitors (NMs) considered here (Table 1) as a function of the modulation potential ϕ for the average R_c for each NM. The values for Sanae64 are divided by 2.2 for a better visibility.

described above) and the measured NM count rates N, and define the scaling factor κ at time t (either monthly or daily resolution) as the ratio between theoretical and measured count rates

$$\kappa(t) = \frac{N^*(t)}{N(t)}. \tag{9}$$

We determine the mean scaling factor κ_j of NM station j as the average of monthly κ values

$$\kappa_j = \langle \kappa_j(t) \rangle. \tag{10}$$

These mean scaling factors are listed in Table 1 along with their standard deviations σ_κ. Different NM stations have different scaling factors. Kerguelen, Newark and Oulu NMs have a scaling factor close to unity, viz. their registration efficiency is close to the nominal one. Kiel and McMurdo have κ values of roughly 1.2–1.3, while Inuvik, Novosibirsk, Sanae64 and Thule have κ values of about 1.6–1.7, and Moscow the largest value of about $\kappa \approx 1.9$. In all cases, $\kappa \geq 1$, implying that the count rate of real NMs is not higher than that of an ideal detector. The exact reasons for different scaling factors are unknown, but they include rescaling/normalization of the datasets, and instrument set-up differences. In particular, former Soviet NMs are equipped by CNM-15 counters which are ≈15% less effective than the BP28 counters used in the standard NM64 (see more details in Gil et al., 2015).

2.5. Merit Function

As the merit function to be minimized, we used the normalized root mean squared error (RMSE) for $X = 10$ stations (Table 1) for each moment t:

$$M(t) = \sqrt{\frac{1}{X}\sum_{j=1}^{X}\left(1 - \frac{\kappa_j N_j(t)}{N_j^*(\phi(t), h)}\right)^2}. \tag{11}$$

By using station-specific mean κ_j, we obtained the best-fit $\phi(t)$ value for each time period (daily and monthly) as the minimum of the merit function. Examples of such determination are shown in Figure 4: by computing the

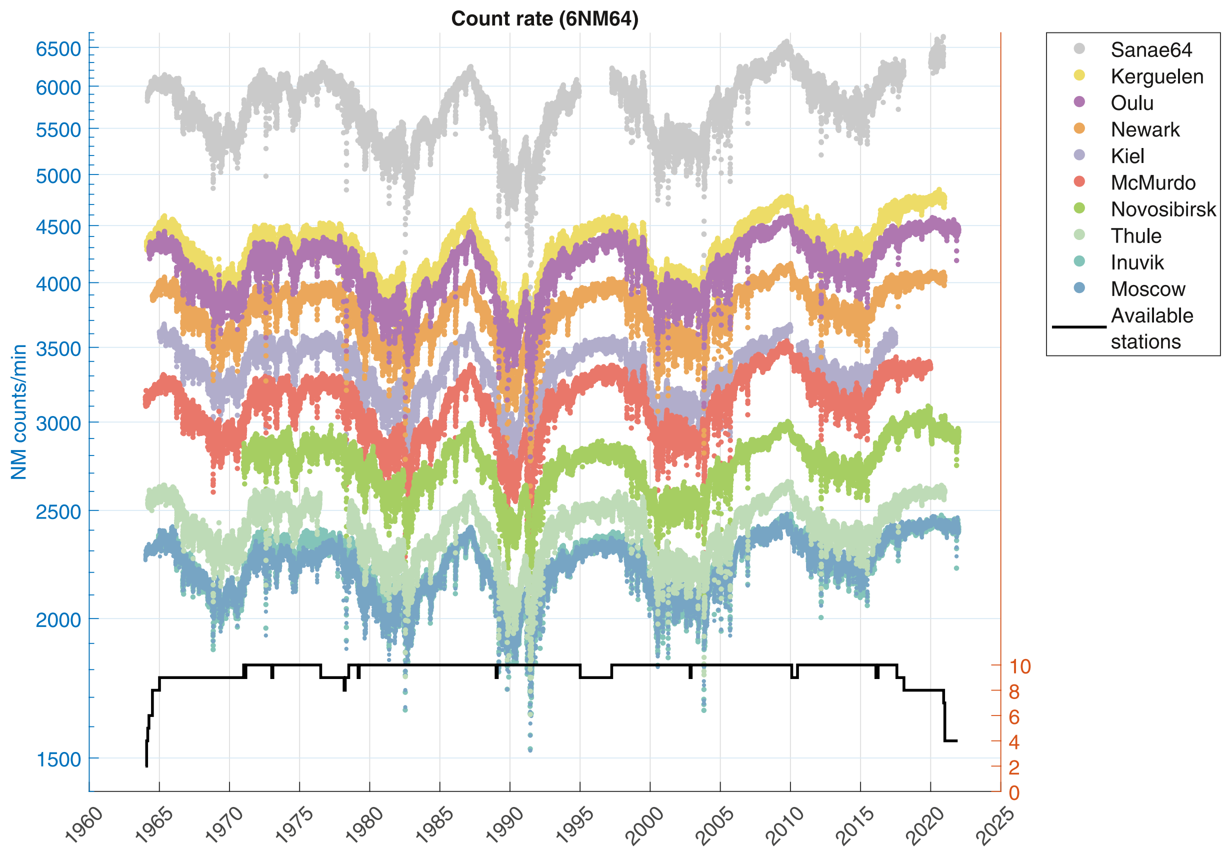

Figure 3. Measured daily count rates *N* (in counts/min, left *Y*-axis) reduced to 6NM64, of the 10 neutron monitors (NMs) used in this study. Note that Inuvik and Moscow values overlap in the plot. The black line represent the monthly number of operational NMs (right *Y*-axis).

merit function for different values of ϕ, the optimum ϕ is determined which corresponds to the minimum values of the merit function. For each individual NM, the minimum $M = 0$, but for the ensemble, the merit function M has a finite positive minimum. All NMs have equal weights here as the statistical noise is negligible for the daily averaging, and it is hardly possible to account for their intrinsic uncertainties caused, for example, the stability of the high-voltage power suppliers, indoor climate control, accuracy of the barometric pressure corrections. The minimum value of the RMSE merit function can also be used as an error estimate as investigated below.

3. Long-Term Modulation Potential ϕ

We have reconstructed the long-term modulation potential ϕ from NM data by minimizing the merit function (Section 2.5), on both daily and monthly timescales. The values of the obtained ϕ-series are available in Tables S1 and S2. The reconstructed series of ϕ is presented in Figure 5a for daily (gray dots) and monthly (yellow line) resolutions alongside with the monthly U17 series (magenta curve, almost invisible behind the yellow curve). Daily values show large variations compared to the smoother monthly series. As an example, Figure 6 shows ϕ values in both daily and monthly resolutions for the year 1991 which was an active year with several activity bursts on the Sun, particularly during March, June–July and late October. During these periods, the daily values of ϕ may significantly deviate from the monthly means, by up to 300 MV.

Figure 5b shows the difference between the monthly ϕ-values obtained here and the U17 series. The difference remains fairly small, mostly within ±20 MV, comparable to the formal errors in U17, except for a few single-point large peaks reaching about 40 MV in September and October of 1989, the period characterized by strong solar disturbances, FDs and GLEs (e.g., Cane & Richardson, 1995). A notable step-like dip of about −20 MV in the difference during 2017–2019 is caused, most likely, by a smaller number of NMs used in the U17 data set to extend it after 2017 (see also discussion below). This shortcoming is fixed in the reconstruction presented here as we use the full NM data set.

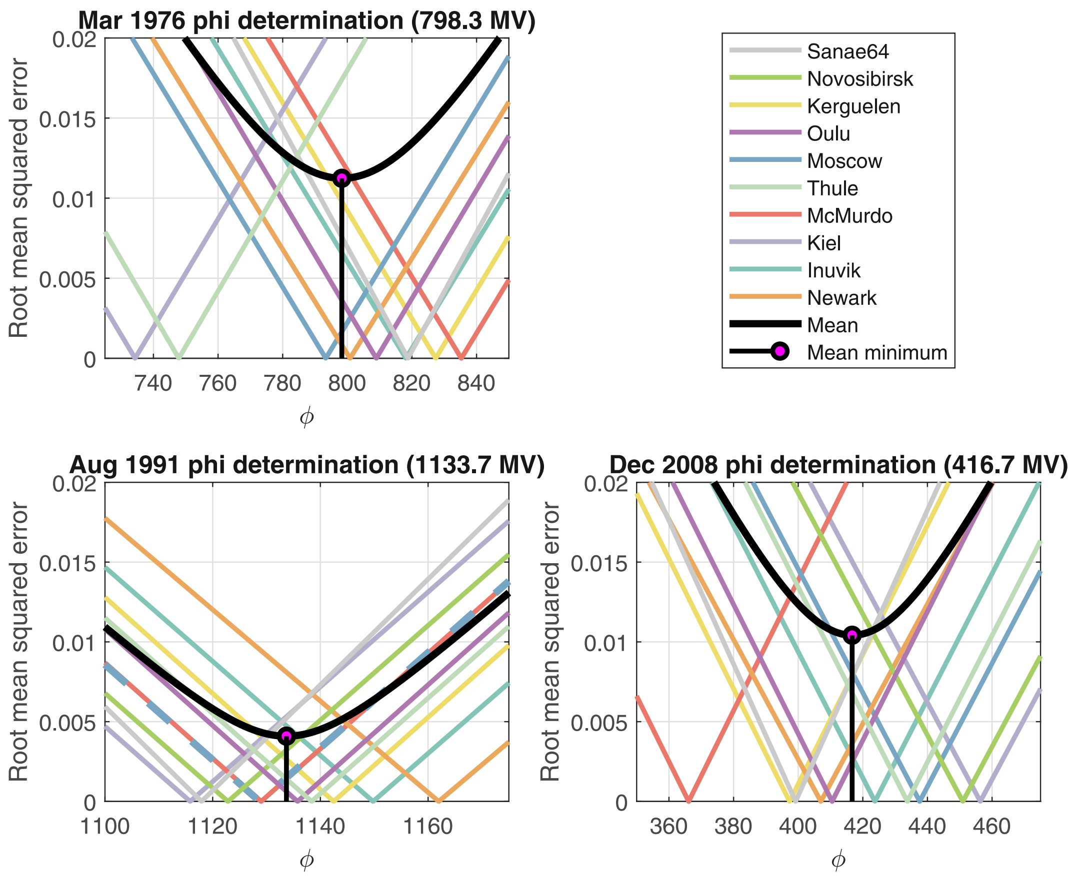

Figure 4. Examples of the merit function M (Equation 11) as a function of the modulation potential ϕ for April 1970, August 1991, and December 2008. Colored dashed curves correspond to individual neutron monitors (NMs), while the thick solid black curves represent the merit function M for the ensemble of 10 NMs. The magenta dots depict the minimum values of M_{min} whose X-axis value determines the best-fit modulation potential ϕ, and whose Y-axis values can be used as an error estimate.

Figure 5c shows the daily and monthly values of the merit function M, which can serve as a measure of the intrinsic uncertainty of the reconstruction, related to the difference between individual NMs. The M values vary typically between 0.005 and 0.015 with the mean value of about 0.01. The merit function exhibits a weak solar-cycle-scale variations, but they are not systematic, with M-values co-varying with ϕ during 1978–1995 and anti-correlating during 1995–2020. This suggests that the force-field may not perfectly describe the GCR spectrum, but the imperfectness is small.

Another interesting feature is related to several periods of a pronounced annual variability of the merit function. One period was in 1964–1973 that was produced by the Oulu NM which, at that time, had a flat roof with snow accumulation during winter months (e.g., Tanskanen, 1968). This was stopped in 1974 when the Oulu NM was moved to a dedicated building with a pyramid-shaped roof. Intermittent annual variability can also be seen, for example, in 1975–1977, 1996–1998, and 2007–2011, viz. during the solar-cycle minimum times. This weak annual periodicity in M may be caused by a seasonal variation in NM efficiency for Newark or Thule NMs (Evenson et al., 2005, also John Clem and Paul Evenson, personal communications, 2022), or by a real small anisotropy of GCR related to the Earth's orbit and heliospheric asymmetry (Jeong & Oh, 2022).

Some specific events can also lead to pronounced errors. For example, the Newark NM had anomalous count rates around 13 February 1994 following the FD on 06 February 1994. Also, slow drifts in the sensitivity of individual NMs can cause uncertainties, as discussed later.

10.1029/2023JA031352

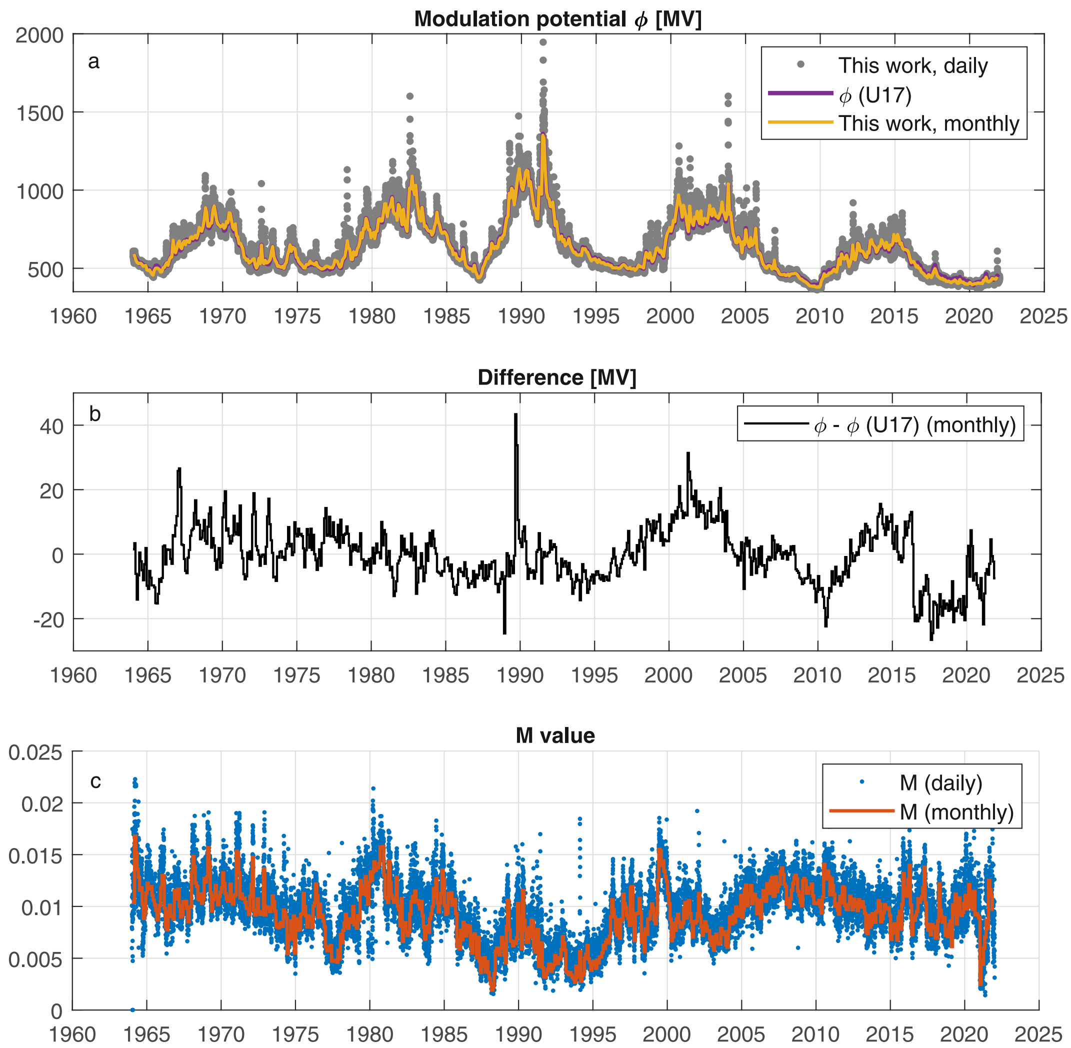

Figure 5. Panel (a) Present reconstruction of the modulation potential ϕ (in MV) for daily (gray dots) and monthly (yellow line) resolution, in comparison with the monthly ϕ_{U17} series (magenta curve, almost invisible behind the yellow one). Panel (b) Difference between the monthly ϕ values of this work and U17. Panel (c) Values of the merit function M at daily (blue dots) and monthly (red curve) resolution.

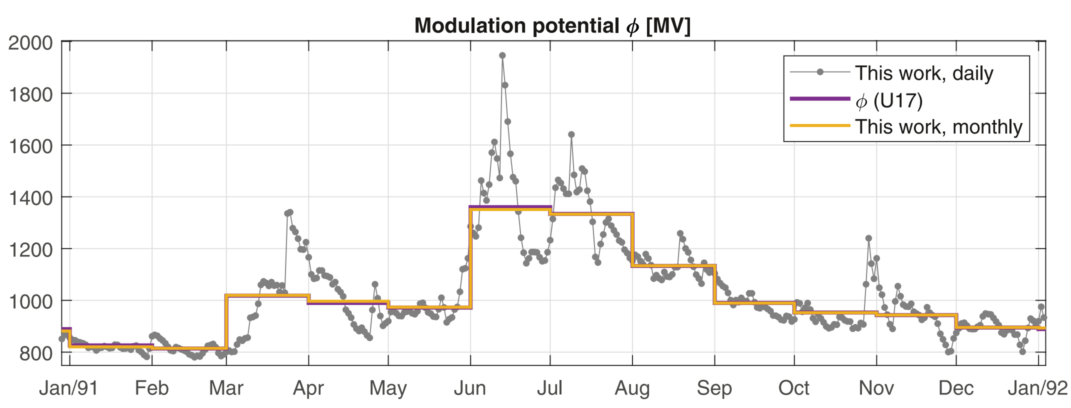

Figure 6. Zoom into Figure 5a for the year 1991.

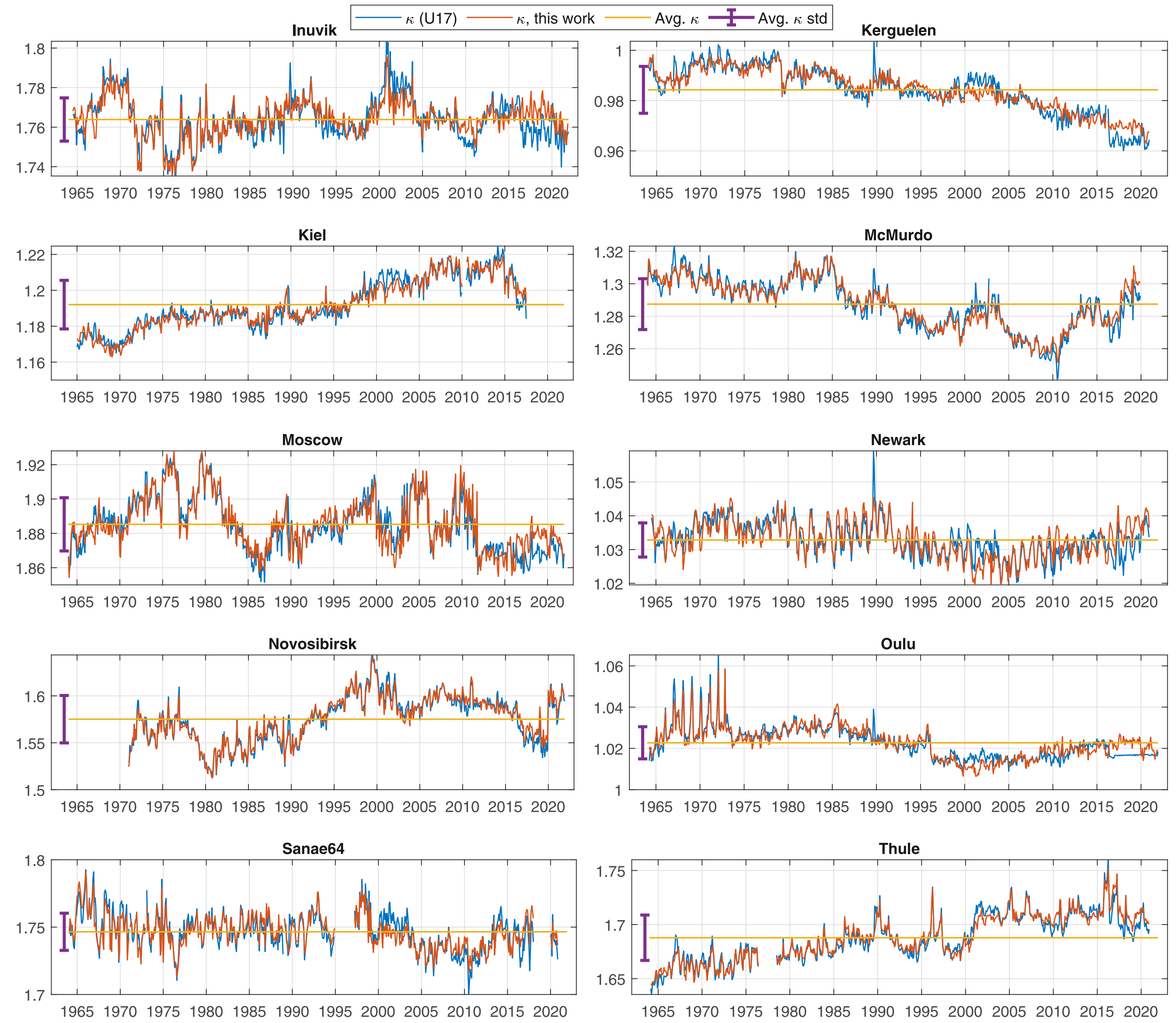

Figure 7. Scaling factor κ computed with the previous (blue U17 curves) and present (red curves) monthly ϕ reconstructions. Yellow lines and magenta bars denote the mean values of κ and its standard deviation level, respectively, as enter Table 1.

3.1. Validation of Scaling Factors

Using the reconstructed series of the modulation potential ϕ, we can study how the station-specific scaling factors κ (Equation 9) vary in time. In Figure 7, the time series of monthly scaling factors are shown as calculated using both the present ϕ and previous (U17) reconstructions. The formal scaling factors of all NMs depicts some variability at different timescales, including long-term trends. Note that scaling factors of the analyzed NMs do not depict a pronounced solar-cycle variability, which implies that the changes in κ are caused by internal causes and not by incorrectly accounted solar modulation. Some stations, that is, Inuvik, Newark, Oulu, and Sanae64, appear fairly stable throughout the decades, while some others have long-term trends in κ, as Kerguelen, Kiel, McMurdo, and Thule. Exact reasons for these trends are not known, but they are most likely related to the station operation. Moscow and Novosibirsk NMs exhibit incoherent variability at decadal timescales.

The annual periodicity at Oulu NM during 1964–1973 is clearly seen in Figure 7 with enhanced κ-values during winter months due to the snow accumulation on the roof (Tanskanen, 1968). Newark and Thule also exhibit weak seasonal variations, with Newark being more systematic and Thule more intermittent. In all these cases, the variations do not exceed a few percent. The small systematic difference between κ-values after 2017 for Kerguelen,

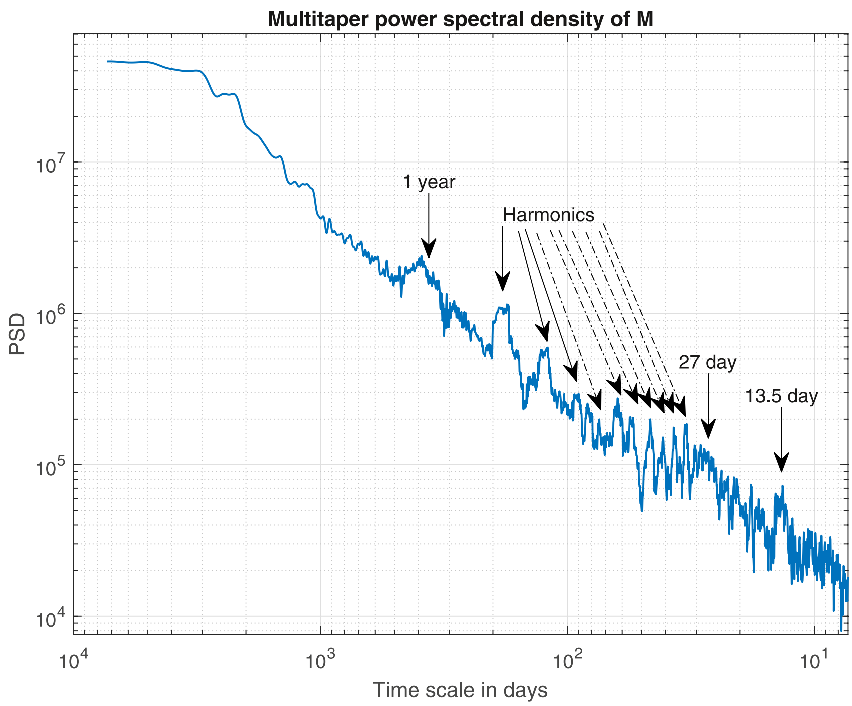

Figure 8. Power spectral density of the daily series of the merit function *M*, calculated using the multitaper method. Notable periodicities of 1 year and 27 days, along with their harmonics, are indicated by arrows.

Moscow and Oulu are related to the fact that only these stations were used in the extension of the U17 series, while here we employ all the 10 stations.

3.2. Power-Spectrum of the Merit Function

The merit function M serves as a measure of intrinsic uncertainties of the reconstruction. Here we check if this uncertainty contains any significant systematic components related to, for example, inappropriate use of the force-field approximation throughout the entire duration or during specific periods. We calculated the power spectral density (PSD) of the daily merit function M depicted in Figure 5. Figure 8 shows the PSD estimated by the Multitaper method with 9 tapers. This method produces a PSD with less noise than other methods by employing orthogonal taper windows (for more details, see Thomson, 1982; Väisänen et al., 2019).

A notable peak corresponds to the annual variation, followed by harmonic peaks at 1/2 − year, 1/3 − year, 1/4 − year and higher harmonics, as indicated by arrows in Figure 8. The annual variability may be due to the Earth's orbital asymmetry (e.g., Jeong & Oh, 2022) or to seasonal effects of individual stations, as discussed above.

Another observable, albeit small, periodicity in the PSD is at about 27 days and its harmonic at 13.5 days. This is most likely related to the synodic solar rotation period, which can cause recurrent variations of the cosmic-ray intensity due to fast solar-wind streams and corotating regions that are most pronounced during the declining and minimum phase of solar cycle as observed in space-borne data (Aguilar et al., 2021).

The presence of these variations in the uncertainties (M-values) may be related to the fact that the force-field model is based on a spherically symmetric heliosphere and may not properly account for the helio-longitudinal asymmetries. This indicates that the daily modulation potential may have some inherent uncertainty, which should be considered when using the daily values. We note that these are not necessarily true periodicities of the cosmic-ray flux but rather intrinsic inconsistency in the force-field spectral reconstruction using multi-NM datasets. On the other hand, this uncertainty is small, typically within 1%–2% as seen in Figure 5c. It is also essential to point out that this PSD analysis does not clearly determine the causes or contributions of periodic variations in the signal.

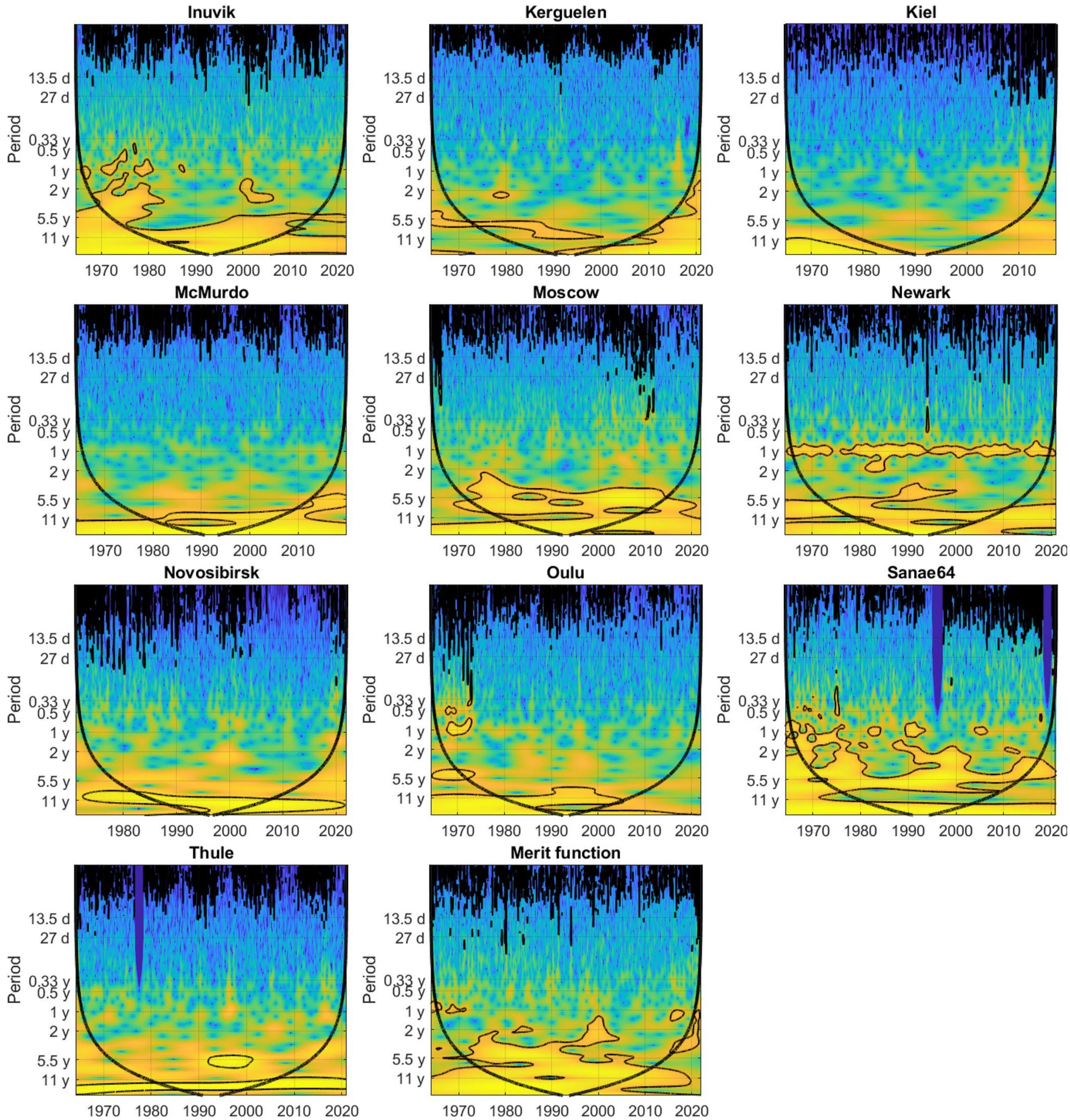

Figure 9. Wavelet scalograms (Morlet with $k = 6$) of the daily station-specific scaling factors and the merit function, as identified by a title on top of each panel. Y-axis represents the timescale in years and X-axis corresponds to the time where the wavelet is centered on. Red curves bound the cones of influence beyond which the wavelet results are unreliable. The black lines bound the 95% confidence level calculated against AR1 noise.

3.3. Wavelet Analysis of NM Station Scaling Factors

We have checked the stability of individual NM stations by analyzing the time variability of their individual scaling factors. We performed this via a wavelet analysis of daily station-specific κ-series, using the Morlet wavelet with $k = 6$ (see Grinsted et al., 2004, for more details) and depicted the related scalograms in Figure 9. The black lines bound the 95% confidence level against AR1 noise. Figure 9 also includes the wavelet scalogram of the merit function M.

Table 2
Dates and Strengths (Maximum Daily Drop in Count Rate Averaged Over All Analyzed Neutron Monitors) of Forbush Decreases Analyzed Here

15 February 1978, 8.12%	02 May 1978, 6.96%	14 July 1982, 12.98%
24 March 1991, 8.66%	27 February 1992, 6.28%	12 April 2001, 8.09%
11 September 2005, 8.67%	09 March 2012, 6.44%	04 November 2021, 5.26%

Figure 9 shows some power at the period of about 11 years, corresponding to the solar cycle, at Inuvik, Kerguelen, McMurdo, Newark, Oulu, Novosibirsk and Thule NMs. Power at the second harmonic of this solar cycle period (about 5.5 years) can also be observed intermittently in some cases, for example, Inuvik, Kerguelen, Moscow, Sanae64 and Thule. Significant power at above 2 years is observable in Inuvik and Sanae64, which might be the third harmonic of the solar cycle.

Notable power for many stations can be observed at the period of 1 year and its second harmonic of 0.5 years. The 1-year period appears as a statistically significant periodicity consistently only in the Newark NM and intermittently in Inuvik, Oulu and Sanae64. For Oulu the second harmonic and shortly even the third harmonic is also significant during the known period of rooftop snow (see discussion above). This power also leads to a similar intermittent annual periodicity of the merit function.

A faint wavelet power band at 27-day solar rotational period can be observed at McMurdo and poorly at Thule stations, but they are insignificant against the AR1 red noise. This indicates that the effect of the 27-day solar rotation is quite low on the station scaling factor values and therefore to the modulation potential. Lower-period variations have varying degree of significance, which for many stations intermittently change according to the solar cycle.

The wavelet power of the merit function is a combination of the wavelet power of the station scaling factors, as expected by its construction. This emphasizes the fact that the value of the merit function and therefore the inherent error present in the modulation potential result is a combination of station-specific uncertainties, that is, improvements in data quality that would bring the scaling factors closer to a constant values will also directly improve the accuracy of the modulation potential estimate.

Overall, the wavelet power analyzed here further indicates that variations in the scaling factors leak intermittently into the merit function, albeit the effect is small, within a few %.

3.4. Possible Relation Between M and ϕ During FDs

The question of whether the force-field approximation is valid during major FDs is important for the applications based on this parameterization. Although the validity of the force-field approximation has been generally confirmed for FDs (Usoskin et al., 2015), it is unclear how large the related uncertainties in the modulation potential, as quantified in M-values, are during these disturbances. For this analysis, we have selected nine major FDs which reduced the daily count rates of high-latitude NMs by more than 5% (see Table 2). Figure 10 shows a scatter plot of the daily values of $\Delta M \equiv M - M_0$ as a function on $\Delta\phi \equiv \phi - \phi_0$ during the duration of the FD, where the subscript 0 denotes the values averaged over 3 days preceding the FD. Figure 10 shows that the values of ΔM are independent of $\Delta\phi$ during the FD date, implying that the quality of the reconstruction is not related to the strength of the FD. Even for the strongest FDs where the formal value of the modulation potential increases by 400–600 MV, there is no observable loss of accuracy. Thus, the modulation potential applies well also during the FDs, which confirms the earlier finding by Usoskin et al. (2015).

Next, we depict in Figure 11 a scatter plot of daily M-values as a function of ϕ for the whole data set. Despite a wide scatter, there is no notable trend in the relation, implying that the modulation potential works equally well for the full range of solar-activity levels, from solar minima with $\phi < 400$ MV up to strong FDs with $\phi > 1400$ MV. The black curve represents the running mean of M over 200 ϕ points and, again, shows no statistically significant trend.

4. Conclusions

In this study we have employed a new method to reconstruct the heliospheric modulation potential ϕ at monthly and daily resolution. The method is based on the simultaneous fit of the most reliable NM data for a given

10.1029/2023JA031352

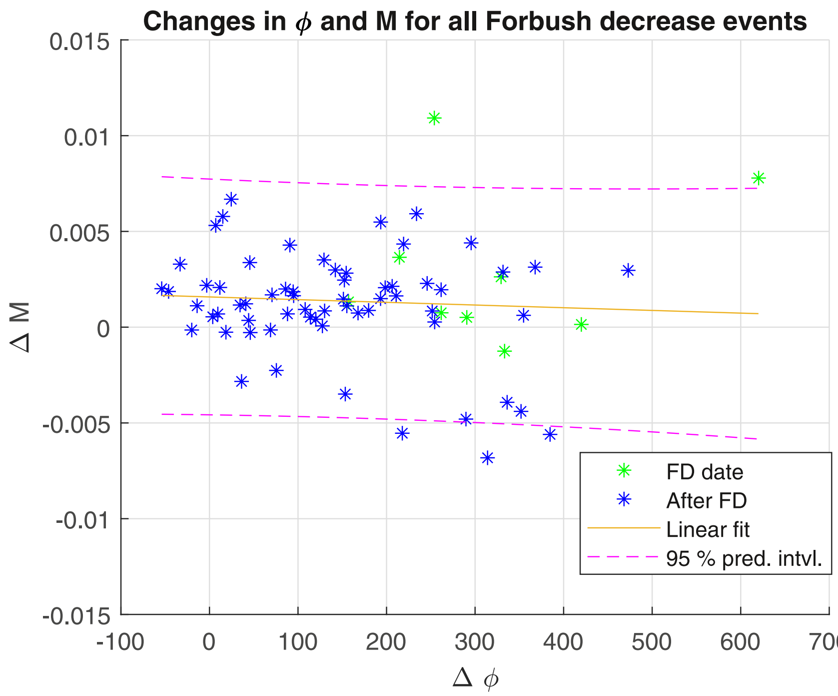

Figure 10. Scatter plot of ΔM versus $\Delta\phi$ for the analyzed Forbush decreases (FDs). Green and blue asterisks correspond to the deep phase and daily recovery of the FDs (over 7 following day), respectively. The yellow and magenta dashed lines represent the best linear fit and the 95% prediction limit, respectively.

day (month) using a single modulation-potential ϕ value which minimizes the merit-function value M. We also computed station-specific scaling factors κ that take into account all discrepancies and non-ideality of the real detectors. The time evolution of the scaling factors was used to examine the temporal stability of each NM station. Even though the 10 most stable NMs have been analyzed here, several of them depict a systematic long-term

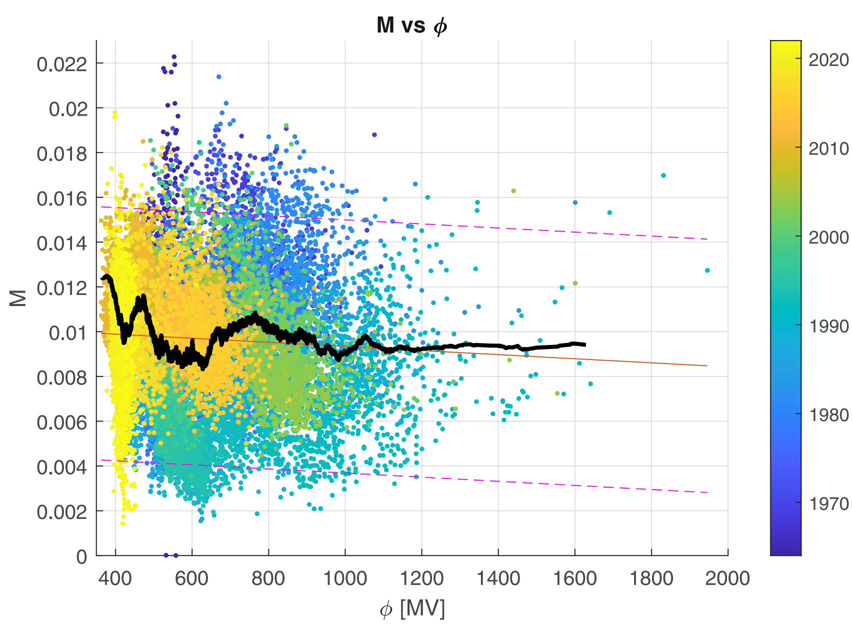

Figure 11. Scatter plot of all daily values of $M(t)$ as a function of $\phi(t)$. The point color represents the time according to the color scheme on the right. The black curve denotes a 200-point running mean along the ϕ-axis. Orange solid and magenta dashed lines depict the best linear fit and the 95% prediction limit, respectively.

trend in the scaling factor by up to ±5% (Kerguelen, Kiel, McMurdo, Moscow, Novosibirsk, Thule), while others (Inuvik, Newark, Oulu, Sanae64) remain fairly stable throughout the decades, within a few percent.

The analysis of the variations of the merit function yields that the applied method is stable, with the mean RMSE being around 1%, containing only marginal periodic variations at periods of 1 year and 27 days. The annual periodicity is notable for a couple of stations (Newark, Oulu) and is very likely due to local effects, such as rooftop snow or unstable indoor temperature. A small asymmetry of GCR in the vicinity of Earth may also contribute to the annual variation of the merit function. The 27-day period is most likely related to the Sun's synodic rotational period and reflects the effect of recurrent fast solar wind streams and corotating interaction regions. Overall, the related uncertainties are quite small. According to the temporal variation of scaling factors shown in Figure 7, the force-field-based reconstruction agrees with the data from high-latitude stable NMs within few % accuracy. We have also shown that the accuracy, as quantified by the merit function M, is not worsened even during strong FDs.

The new monthly reconstruction of the modulation potential is close to the monthly potential values presented earlier by Usoskin et al. (2017), but is based on an updated methodology with the use of a new, better validated NM yield function and a better choice of the used NM stations and fixes some shortcomings of the U17 approach in particular, by using a daily resolution and improving decimal accuracy of the data. The most important update is for the period after 2017, when the previous reconstruction was based on a smaller number of stations and therefore less reliable.

The new method is suitable to be rescaled to a larger number of stations, which would further improve accuracy. Furthermore, if the reliability of individual stations could be assessed, additional weighting can also be introduced to the RMSE computation. Any future corrections to the current data set can also be easily implemented. The method is also suitable for computing hourly or even higher resolution versions of ϕ, if needed.

Data Availability Statement

The obtained reconstructions are tabulated in the Supporting Information S1 and published freely through Fairdata.fi -repository (citation: Väisänen et al. (2023)) with CC4 BY-NC license and data physically stored in University of Oulu's Cosmic ray station servers. Data will also be made available in https://cosmicrays.oulu.fi/phi/phi.html, with updates available in the future.

Acknowledgments

We thank the NMDB and IZMIRAN databases and the teams of the 10 NM stations (see Table 1) used in this study. This work was also partly supported by the Academy of Finland (projects ESPERA, Grant 321882, and QUASARE, Grant 330064), and University of Oulu (Project SARPEDON).

References

Aguilar, M., Cavasonza, L. A., Ambrosi, G., Arruda, L., Attig, N., Barao, F., et al. (2021). Periodicities in the daily proton fluxes from 2011 to 2019 measured by the Alpha Magnetic Spectrometer on the International Space Station from 1 to 100 GV. *Physical Review Letters*, *127*(27), 271102. https://doi.org/10.1103/PhysRevLett.127.271102

Alken, P., Thébault, E., Beggan, C. D., Amit, H., Aubert, J., Baerenzung, J., et al. (2021). International Geomagnetic Reference Field: The thirteenth generation. *Earth Planets and Space*, *73*(1), 49. https://doi.org/10.1186/s40623-020-01288-x

Bieber, J. W., Evenson, P., Dröge, W., Pyle, R., Ruffolo, D., Rujiwarodom, M., et al. (2004). Spaceship Earth observations of the Easter 2001 solar particle event. *The Astrophysical Journal Letters*, *601*(1), L103–L106. https://doi.org/10.1086/381801

Caballero-Lopez, R. A., & Moraal, H. (2004). Limitations of the force field equation to describe cosmic ray modulation. *Journal of Geophysical Research*, *109*(A1), 1–7. https://doi.org/10.1029/2003JA010098

Cane, H. V., & Richardson, I. G. (1995). Cosmic ray decreases and solar wind disturbances during late October 1989. *Journal of Geophysical Research*, *100*(A2), 1755–1762. https://doi.org/10.1029/94JA03073

Cooke, D., Humble, J., Shea, M., Smart, D., Lund, N., Rasmussen, I., et al. (1991). On cosmic-ray cut-off terminology. *Nuovo Cimento C*, *14*(3), 213–234. https://doi.org/10.1007/bf02509357

Corti, C., Bindi, V., Consolandi, C., & Whitman, K. (2016). Solar modulation of the local interstellar spectrum with Voyager 1, AMS-02, PAMELA, and BESS. *The Astrophysical Journal*, *829*(1), 8. https://doi.org/10.3847/0004-637X/829/1/8

Desorgher, L., Flückiger, E. O., Gurtner, M., Moser, M. R., & Bütikofer, R. (2005). Atmocosmics: A Geant 4 code for computing the interaction of cosmic rays with the Earth's atmosphere. *International Journal of Modern Physics A*, *20*(29), 6802–6804. https://doi.org/10.1142/S0217751X05030132

Dumbović, M., Vršnak, B., Temmer, M., Heber, B., & Kühl, P. (2022). Generic profile of a long-lived corotating interaction region and associated recurrent Forbush decrease. *Astronomy & Astrophysics*, *658*, A187. https://doi.org/10.1051/0004-6361/202140861

Engelbrecht, N. E., Effenberger, F., Florinski, V., Potgieter, M. S., Ruffolo, D., Chhiber, R., et al. (2022). Theory of cosmic ray transport in the heliosphere. *Space Science Reviews*, *218*(4), 33. https://doi.org/10.1007/s11214-022-00896-1

Evenson, P., Bieber, J. W., Clem, J., & Pyle, R. (2005). Neutron monitor temperature coefficients: Measurements for BF3 and 3He counter tubes. In *29th international cosmic ray conference (ICRC 29)* (Vol. 2, p. 485).

Gil, A., Usoskin, I. G., Kovaltsov, G. A., Mishev, A. L., Corti, C., & Bindi, V. (2015). Can we properly model the neutron monitor count rate? *Journal of Geophysical Research*, *120*(9), 7172–7178. https://doi.org/10.1002/2015JA021654

Gleeson, L. J., & Axford, W. I. (1968). Solar modulation of galactic cosmic rays. *The Astrophysical Journal*, *154*, 1011. https://doi.org/10.1086/149822

Grinsted, A., Moore, J. C., & Jevrejeva, S. (2004). Application of the cross wavelet transform and wavelet coherence to geophysical time series. *Nonlinear Processes in Geophysics*, *11*(5/6), 561–566. https://doi.org/10.5194/npg-11-561-2004

Herbst, K., Kopp, A., Heber, B., Steinhilber, F., Fichtner, H., Scherer, K., & Matthiä, D. (2010). On the importance of the local interstellar spectrum for the solar modulation parameter. *Journal of Geophysical Research: Atmospheres*, *115*, D00I20. https://doi.org/10.1029/2009JD012557

Jeong, J., & Oh, S. (2022). Seasonal trends of the cosmic ray intensity observed by 16 neutron monitors for 1964-2020. *Advances in Space Research*, *70*(9), 2625–2635. https://doi.org/10.1016/j.asr.2022.02.052

Jokipii, J. R., & Levy, E. H. (1977). Effects of particle drifts on the solar modulation of galactic cosmic rays. *The Astrophysical Journal Letters*, *213*, L85–L88. https://doi.org/10.1086/182415

Koldobskiy, S. A., Bindi, V., Corti, C., Kovaltsov, G., & Usoskin, I. (2019). Validation of the neutron monitor yield function using data from AMS-02 experiment 2011–2017. *Journal of Geophysical Research: Space Physics*, *124*(4), 2367–2379. https://doi.org/10.1029/2018JA026340

Mishev, A. L., Koldobskiy, S. A., Kovaltsov, G. A., Gil, A., & Usoskin, I. G. (2020). Updated neutron-monitor yield function: Bridging between in situ and ground-based cosmic ray measurements. *Journal of Geophysical Research: Space Physics*, *125*(2), e2019JA027433. https://doi.org/10.1029/2019JA027433

Parker, E. (1965). The passage of energetic charged particles through interplanetary space. *Planetary and Space Science*, *13*(1), 9–49. https://doi.org/10.1016/0032-0633(65)90131-5

Poluianov, S., Usoskin, I., Mishev, A., Shea, M., & Smart, D. (2017). GLE and sub-GLE redefinition in the light of high-altitude polar neutron monitors. *Solar Physics*, *292*(11), 176. https://doi.org/10.1007/s11207-017-1202-4

Potgieter, M. (2013). Solar modulation of cosmic rays. *Living Reviews in Solar Physics*, *10*, 3. https://doi.org/10.12942/lrsp-2013-3

Simpson, J. A. (2000). The cosmic ray nucleonic component: The invention and scientific uses of the neutron monitor. *Space Science Reviews*, *93*(1/2), 11–32. https://doi.org/10.1023/A:1026567706183

Tanskanen, P. (1968). Influence of snow on neutron monitor intensity. *Nature*, *219*(5157), 926–927. https://doi.org/10.1038/219926a0

Thomson, D. J. (1982). Spectrum estimation and harmonic analysis. *IEEE Proceedings*, *70*(9), 1055–1096. https://doi.org/10.1109/PROC.1982.12433

Tsyganenko, N. A. (1989). A magnetospheric magnetic field model with a warped tail current sheet. *Planetary and Space Science*, *37*(1), 5–20. https://doi.org/10.1016/0032-0633(89)90066-4

Usoskin, I. G., Alanko-Huotari, K., Kovaltsov, G. A., & Mursula, K. (2005). Heliospheric modulation of cosmic rays: Monthly reconstruction for 1951–2004. *Journal of Geophysical Research*, *110*(A12), A12108. https://doi.org/10.1029/2005JA011250

Usoskin, I. G., Bazilevskaya, G. A., & Kovaltsov, G. A. (2011). Solar modulation parameter for cosmic rays since 1936 reconstructed from ground-based neutron monitors and ionization chambers. *Journal of Geophysical Research*, *116*(A2). https://doi.org/10.1029/2010JA016105

Usoskin, I. G., Gil, A., Kovaltsov, G. A., Mishev, A. L., & Mikhailov, V. V. (2017). Heliospheric modulation of cosmic rays during the neutron monitor era: Calibration using PAMELA data for 2006–2010. *Journal of Geophysical Research: Space Physics*, *122*(4), 3875–3887. https://doi.org/10.1002/2016JA023819

Usoskin, I. G., Kovaltsov, G. A., Adriani, O., Barbarino, G. C., Bazilevskaya, G. A., Bellotti, R., et al. (2015). Force-field parameterization of the galactic cosmic ray spectrum: Validation for Forbush decreases. *Advances in Space Research*, *55*(12), 2940–2945. https://doi.org/10.1016/j.asr.2015.03.009

Väisänen, P., Usoskin, I., Koldobskiy, S., Kähkönen, R., & Mursula, K. (2023). Cosmic ray heliospheric modulation potential. Pauli Väisänen. Retrieved from http://urn.fi/urn:nbn:fi:att:66ac9a04-d16f-48b3-a996-5cbfee1c329b, https://etsin.fairdata.fi/dataset/5d3e6ee0-c75a-42ab-8003-3cb3df5908fa

Väisänen, P., Usoskin, I., & Mursula, K. (2019). Long-term and solar cycle variation of galactic cosmic rays: Evidence for variable heliospheric turbulence. *Journal of Geophysical Research: Space Physics*, *124*(2), 804–811. https://doi.org/10.1029/2018JA026135

Väisänen, P., Usoskin, I., & Mursula, K. (2021). Seven decades of neutron monitors (1951–2019): Overview and evaluation of data sources. *Journal of Geophysical Research: Space Physics*, *126*(5), e2020JA028941. https://doi.org/10.1029/2020JA028941

Vos, E. E., & Potgieter, M. S. (2015). New modeling of galactic proton modulation during the minimum of solar cycle 23/24. *The Astrophysical Journal*, *815*(2), 119. https://doi.org/10.1088/0004-637X/815/2/119